Nanoscale

PAPER

Facile multifunctional plasmonic sunlight harvesting with tapered triangle nanopatterning of thin films†

Giulia Tagliabue, Hadi Eghlidi* and Dimos Poulikakos*

Plasmonic absorbers have recently become important for a broad spectrum of sunlight-harvesting applications exploiting either heat generation, such as in thermal photovoltaics and solar thermoelectrics, or hot-electron generation, such as in photochemical and solid state devices. So far, despite impressive progress, combining the needed high performance with fabrication simplicity and scalability remains a serious challenge. Here, we report on a novel solar absorber concept, where we demonstrate and exploit simultaneously a host of absorption phenomena in tapered triangle arrays integrated in a metal–insulator–metal configuration to achieve ultrabroadband (88% average absorption in the range of 380–980 nm), wide-angle and polarization-insensitive absorption. Furthermore, this absorber is subwavelength in thickness (260 nm) and its fabrication is based on a facile, low-cost and potentially scalable method. In addition, the geometry of our design makes it compatible for both heat and hot electron generation.

Introduction

During the past few years, plasmonic structures have been increasingly employed in various solar light harvesting applications, *e.g.* as light management structures in solar cells,[1,2] nano-scale heat sources in thermal photovoltaic or thermo-electric systems[3,4] and hot-electron generators for photochemical reactions[5,6] or solid-state devices.[7,8] The main promise of plasmonics is the unique capability to fulfill the demanding requirements of such devices which need to be broadband as well as insensitive to light polarization and angle of incidence, and for several novel applications, sub-wavelength in thickness.[9] In addition, a facile[10] and controllable nanofabrication technique is required for realistic applications. Unlike polymer–metal nano-composites,[11–13] which can fulfill some of these requirements, well-defined nanopatterns usually provide access to hot-spots where energy is strongly concentrated and subsequently exploited.[6–8] Aydin *et al.*[14] first introduced a plasmonic broadband absorber taking advantage of multiple resonances in a metal–insulator–metal (MIM) stack with a top silver film consisting of crossed trapezoidal arrays and achieved 71% average absorption within the visible spectrum (400–700 nm).

While different geometries showed further improvements[15] their small scale structuring is attained with difficulty and the upscaling of fabrication methods seems improbable. A different theoretical approach based on conformal transformations has exploited non-resonant nano-focusing at the end of sharp tips or grooves to achieve plasmonic nanostructures with very large absorption cross-sections over a broad spectral range.[16–18] Following a similar principle, Sondergaard *et al.*[19,20] realized a broadband absorber consisting of an array of ultra-sharp convex grooves. Despite impressive results (>87% absorption over 450–850 nm) their design requires extremely narrow features, which are achieved by a cumbersome combination of electron-beam lithography and focused ion-beam milling (also practically impossible to upscale). Moreover, the structure is not sub-wavelength in thickness and the focusing hot-spots are deeply buried into the structure, therefore inaccessible for several light harvesting applications. In this paper, we address these issues by a concept, which exploits various plasmonic absorption phenomena in an array of tapered triangles within an MIM structure. While achieving a near-ideal solar absorber, we are able to fabricate the device with a potentially low-cost and easily accessible method, a must if plasmonic solar harvesting is to become a reality outside the research laboratory.

Results and discussion

The schematic representation of the absorber is given in Fig. 1a and b, where all the relevant geometrical parameters are introduced. The MIM structure is composed of three layers (see Fig. 1a). A 100 nm gold back-reflector and a 60 nm SiO₂ layer were coated successively on a glass coverslip using electron-beam

Laboratory of Thermodynamics in Emerging Technologies, Institute of Energy Technology, Department of Mechanical and Process Engineering, ETH Zürich, CH-8092 Zürich, Switzerland. E-mail: hadi.eghlidi@ltnt.iet.mavt.ethz.ch; dpoulikakos@ethz.ch; Fax: +41 44 632 11 76; Tel: +41 44 632 06 77; +41 44 632 27 38

† Electronic supplementary information (ESI) available: Detailed geometry description; set-up description; literature comparison; surface plasmon polariton dispersion curve; absorption efficiency of an isolated tapered triangle on glass. See DOI: 10.1039/c3nr03273f

evaporation and plasma-enhanced chemical vapor deposition, respectively. A front hexagonal gold pattern was fabricated using nano-sphere lithography (NSL)[21–24] and reactive ion etching (RIE).‡ The schematic top-view of the front pattern is shown in Fig. 1b. R is defined as the radius of curvature of the pattern, and R_{bead} is the radius of the spheres (beads) which are used in the NSL and constitute a closely packed hexagonal array. ΔR is defined as the difference between R and R_{bead}. For $\Delta R > 0$, the front pattern consists of an array of disconnected gold triangles with curved sides. The neighbouring tapered triangles touch each other at a single point when $\Delta R = 0$. Due to overshadowing,[24] experimentally $\Delta R > 0$ can be obtained and fine-adjusted by varying the etching time of the RIE process mentioned above. By doing this we can vary the size of the triangles and the tapering of their tips (2θ, see Fig. 1b). A top view scanning electron micrograph of a created structure is shown in Fig. 1c.

The performance of the proposed absorber is illustrated in Fig. 2b–j, where the measured and calculated absorption
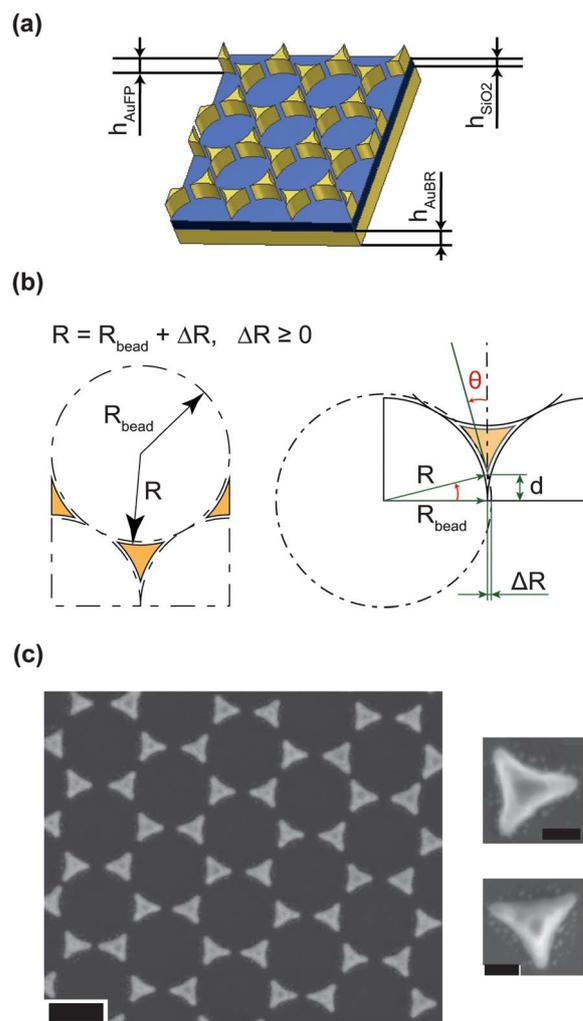

Fig. 1 Geometry of the proposed absorber. (a) Schematic representation of the MIM absorber consisting of a gold back reflector, a SiO$_2$ dielectric spacer, and a patterned gold front layer with thicknesses h_{AuBR}, h_{SiO_2}, and h_{AuFP}, respectively. (b) Definition of the in-plane geometrical parameters of the front gold pattern: R_{bead} is the radius of the spherical beads used in the NSL, and R is defined as the radius of curvature of the pattern. ΔR represents the difference between R and R_{bead} and can be adjusted in the fabrication. 2θ and $2d$ are the tip tapering angle and the distance between two neighboring tips, respectively. (c) Left: top-view scanning electron micrograph of a fabricated structure. Scale bar is 200 nm. Right: magnified top views of single tapered triangles. Scale bars are 50 nm.

‡ *Fabrication procedure details*. Clean glass coverslips (18 × 18 mm) were coated first with a 100 nm gold back reflector (electron beam evaporation) and successively with a 60 nm SiO$_2$ layer (plasma enhanced chemical vapor deposition). The thickness of the dielectric spacer and optical properties of SiO$_2$ and gold layers were always measured using ellipsometry. After cleaning with a 6 : 1 : 1 solution of H$_2$O : NH$_4$OH : H$_2$O$_2$ in an ultrasonic bath for 10 min, the samples were stored for 24 h in ethanol to ensure full hydrophilicity of the glass surface. The hexagonal gold patterns are fabricated using nanosphere lithography (NSL) and etching techniques. First, a closely packed monolayer of polystyrene beads (Sigma Aldrich, diameter 300 nm) is created using dip-coating (see ESI S2† for the set-up): the sample is quickly immersed into a diluted bead solution (1 wt%, 10^{-3} M SDS) and then withdrawn with controlled velocity (≈ 2.5 μm s^{-1}). The humidity is kept constant at $\approx 50\%$. Then, reactive ion etching is used to reduce the bead size (100 sccm Ar, 10 sccm O$_2$, 50 W, 100 μbar). The bead size is controlled by adjusting the etching time. Due to overshadowing in the NSL,[24] zero or short etching times result in disconnected curved triangles ($\Delta R > 0$). The final pattern is created by evaporating 100 nm of gold (after 2 nm Cr adhesion layer) through the bead mask and by successively removing the beads by low power ultrasonication.

Optical Measurements. Absorption measurements are performed using a home-built inverted microscope equipped with an air objective (numerical aperture 0.75) for exciting the sample and collecting the reflected and scattered light and a spectrometer (Princeton Instruments). White light is generated by a xenon lamp and is brought to the set-up with an optical fiber (105 μm core size) in order to improve its spatial coherence. Plane wave excitations with different angles of incidence are achieved by focusing the light beam at different positions on the back focal plane of the objective. The relation **A** = (**I** − **R**)/**I** was used to calculate the absorption spectrum, where **A**, **I** and **R** are the absorption, incident (excitation) and reflected spectra, respectively. The light transmitted through the absorber was negligible. **I** was measured using the reflected spectrum from a broadband silver mirror. This ensures accounting for excitation spectral non-uniformity and loss along the detection path. Furthermore, dark counts of the spectrometer and background spectra were subtracted from all the measured spectra.

Simulations. Primary estimation of optimal dimensions was achieved by performing a large series of full-wave simulations with Lumerical, a commercially available finite-difference time-domain (FDTD) software package, which is very efficient for broadband simulations. However, due to the staircasing errors of FDTD at sharp edges, the final simulations (which include all the results shown in this manuscript) were performed using the COMSOL Multiphysics package (RF module), which is based on the finite element method (FEM). By using symmetry and periodic (for normal excitation) or Floquet (for oblique excitation) boundary conditions the computational domain was reduced to one-fourth of a unit-cell. To model gold in the simulations, we used the optical properties tabulated in Palik's Handbook[25] which agree well with our ellipsometry measurements (see Fabrication procedure details).

spectra are plotted for different values of ΔR. The other geometrical parameters are fixed at $R_{bead} = 150$ nm and $h_{SiO_2} = 60$ nm (see Fig. 2a), and the thickness of the back reflector and the gold triangles are both equal to 100 nm. The overall structure is only 260 nm thick. The numerical simulations are carried out using the COMSOL Multiphysics package (RF Module)‡ and the absorption measurements were performed using a home-built inverted microscope. Collimated white light was used for excitation and the absorption spectrum, **A**, was calculated as **A** = (**I** − **R**)/**I**, where **I** and **R** are the incident (excitation) and reflected spectra, respectively. The light transmitted through the absorber was negligible.‡

Both simulation and experimental data suggest that decreasing ΔR (equivalently decreasing 2θ) increases the

absorption bandwidth while maintaining reasonably high absorption within the bandwidth. The best experimental result in terms of broadness is obtained at $\Delta R \approx 2$ nm (see Fig. 2j), for which the neighbouring tapered triangles' tips are at the closest distance but still separated. Here, absorption stays above 85% within the spectral range of 380–850 nm and slowly drops to 70% at 980 nm. We reach an average absorption slightly higher than 88% within the spectral range of 380–980 nm. The numerical results in Fig. 2b show a rapid increase in the absorption bandwidth as ΔR approaches zero (equivalently, the distance between the tips of neighbouring triangles as well as θ decrease). As mentioned above, ΔR can be controlled with

nanometer resolution by using a slow enough etching process. While the fabrication relies on a facile method, the results show the potential of the proposed concept to easily adjust the absorption bandwidth and achieve a near-ideal absorber.

Angular insensitivity is one of the important properties of an ideal absorber. To assess the angular sensitivity of our absorber we illuminated it with plane waves at different angles of incidence. We obtained this by focusing the excitation light at different positions on the back-focal plane of the objective with which we were able to reach angles up to 48 degrees (numerical aperture, NA = 0.75). The measured absorption spectra for the best experimental case (Fig. 2j) for incidence angles from 0 to 45
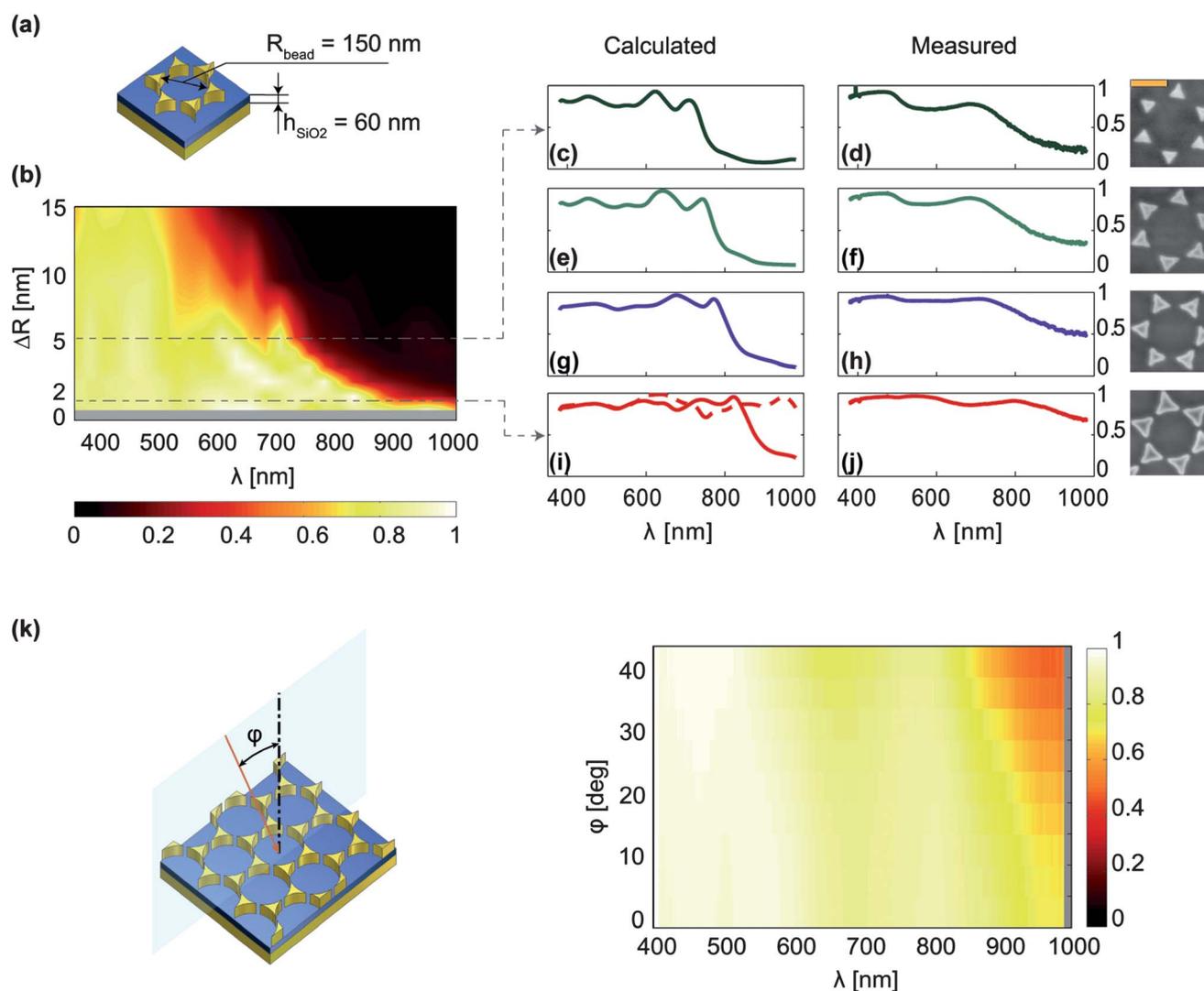

Fig. 2 Measured and calculated absorption spectra of the absorbers. (a) Schematic representation of a unit cell of the absorber. In all studied cases R_{bead} and h_{SiO_2} are kept constant while ΔR is varied. (b) Simulated absorption plotted as a function of wavelength λ and ΔR. The absorption bandwidth is very large for small positive ΔR's. Simulations for ΔR between 0 nm and 1 nm turned out to be very challenging and beyond our capabilities (gray area). (c–j) Calculated (left column) and measured (right column) absorption spectra for different values of ΔR; from top to bottom: $\Delta R = 6$ nm (c and d), 4 nm (e and f), 3 nm (g and h), 2 and 1 nm (i and j). The spectral response for the case of small ΔR becomes very sensitive to slight changes in this value. Therefore, the ultra-broadband absorption behavior observed in (j) can be viewed as the result of a superposition of different cases with slightly different ΔR values, two typical values of which are calculated in (i): solid ($\Delta R = 2$ nm) and dashed ($\Delta R = 1$ nm) lines. The SEM pictures on the right show unit cells of the fabricated structure for each case. Scale bar is 200 nm. (k) Left: schematic drawing of the absorber with light incident at an angle φ. Right: experimentally measured absorption plotted as a function of wavelength λ and angle of incidence φ. The objective used for excitation (NA = 0.75) allowed excitation angles up to $\varphi = 48°$.

degrees are summarized in Fig. 2k. The results show that a broad absorption spectrum is preserved even at large angles of incidence.[26] Finally, our design concept is inherently polarization insensitive at normal incidence. This is due to the geometrical planar symmetries that it contains. In addition, the measurements, which are performed with unpolarized light, and the simulations (not shown for brevity) confirm a similar insensitivity for angles away from the normal.

The broadband absorption behaviour of our design is the collective result of a number of plasmonic absorption events. These events occur at different locations of the spectrum and, after appropriate choice of the geometrical dimensions, piece together a continuous absorption band. To assess the impact of the dielectric spacer thickness, in Fig. 3a we show the calculated absorption spectra for different values of h_{SiO_2}. All of the other geometrical parameters are kept constant ($R_{bead} = 150$ nm, $h_{Au,FP} = 100$ nm, $\Delta R = 2$ nm, see Fig. 2a). The horizontal dashed line shows the situation that we have in the experiment, $h_{SiO_2} = 60$ nm (Fig. 2j), which leads to very high absorption over the

entire absorption spectrum. Moving away from this optimal thickness leads to the appearance of spectral bands with high reflection in the visible range. To understand the origin of the broadband absorption, we studied the field distributions inside the dielectric layer on two horizontal cross-sections, close to the top pattern and close to the back reflector. Fig. 3d shows magnetic field enhancement profiles at four absorption peaks indicated by P_1–P_4 in Fig. 3a.

At P_1 ($\lambda = 470$ nm) we note that the electromagnetic energy is concentrated close to the back-reflector. This indicates that the absorption at this wavelength originates from the grating-mediated coupling of electromagnetic field to the surface plasmon polariton (SPP) excited at the interface between the SiO_2 layer and the gold back reflector.[27] Our analytical calculations for the simplified three-layer (air–SiO_2–gold) structure predict the grating coupled SPP (corresponding to the grating period $= 2R_{bead} = 300$ nm) at $\lambda = 498$ nm (see ESI, Fig. S2†), which is close to the observed resonance. This absorption resonance only slightly blue-shifts as the value of h_{SiO_2}
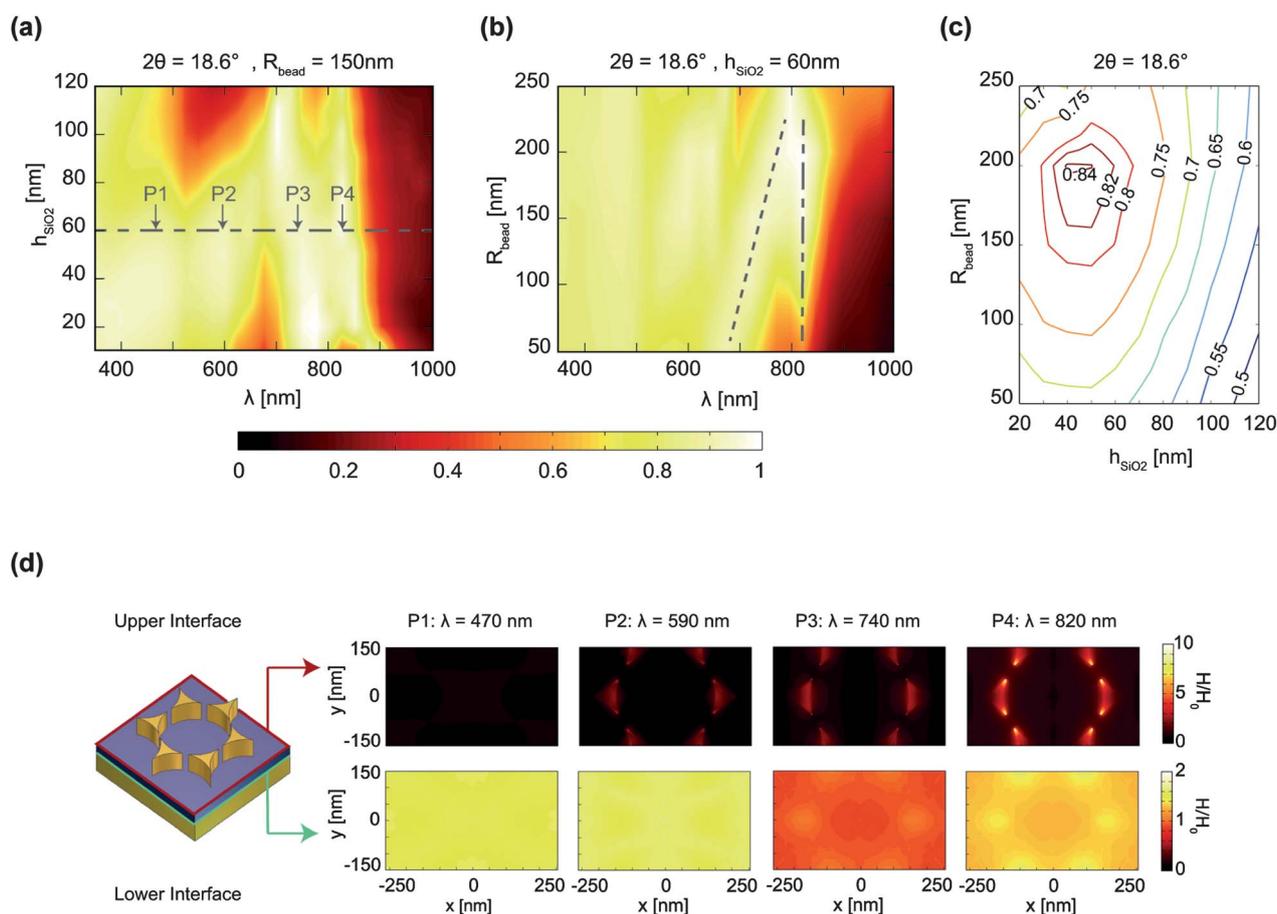

Fig. 3 Absorption spectra vs. geometrical parameters and field profiles. (a) Simulated absorption spectrum as a function of h_{SiO_2} for $R_{bead} = 150$ nm and $h_{AuBR} = h_{AuFP} = 100$ nm. The dashed line indicates the best case, which also corresponds to the experimentally realized absorber. The arrows P_1–P_4 indicate the position of the main absorption peaks. (b) Simulated absorption spectrum as a function of R_{bead} for $h_{SiO_2} = 60$ nm and $h_{AuBR} = h_{AuFP} = 100$ nm. The eye-guiding dotted and dotted-dashed lines show the change in the absorption peaks corresponding to P_3 and P_4, respectively. (c) Contour plot showing total absorption of sunlight, A_{tot}, as a function of geometrical parameters R_{bead} and h_{SiO_2}. In order to compare similar tip geometries, $\Delta R/R_{bead}$ is kept constant and equal to 0.0133 ($2\theta = 18.6°$). Absorption is calculated within the spectral range of 350–1000 nm assuming the solar irradiance for the standard AM1.5 (air mass) spectrum. (d) Normalized magnetic field (H) profiles at two cross-sections within the SiO_2 layer for the cases specified by P_1–P_4 in (a) (upper cross-section: interface between the front Au pattern and the SiO_2 layer; lower cross-section: interface between the SiO_2 layer and the gold back reflector).

increases. The absorption peak at P_2 ($\lambda = 590$ nm) is substantially influenced by h_{SiO_2} and becomes weaker for SiO_2 thicknesses away from 60 nm. This peak red-shifts as h_{SiO_2} increases and is a result of a dipole–dipole interaction between the triangles and the gold back reflector.[28] The field profiles in Fig. 3d (P_2) verify the contribution of both triangles and the back reflector to this resonance. The absorption event at P_3 mainly originates from the localized surface plasmon (LSP) resonance of the individual tapered triangles. Our simulations of an isolated tapered triangle on a glass substrate reveal a dominant absorption peak for λ close to 720 nm (see ESI, Fig. S3†) which complies with the observed resonance at P_3. The position of this absorption peak is only slightly influenced by h_{SiO_2} and the weak field enhancement on the back reflector confirms the dominant contribution of the individual triangles to the resonance (see Fig. 3d (P_3)). Absorption at P_4 originates from the presence of the tips where energy is accumulated and dissipated. This is evident from the strong field enhancement at the tips shown in Fig. 3d (P_4).

Further evidence for the above-mentioned attributes is given in Fig. 3b, where calculated absorption spectra are plotted as a function of R_{bead}. Here, by maintaining the ratio $\Delta R/R_{bead}$ constant, we are able to keep the tip angle, 2θ, constant and equal to 18.6°. Other geometrical values are $h_{SiO_2} = 60$ nm and $h_{Au,FP} = 100$ nm. The two eye-guiding lines show the variation of the position of the resonances corresponding to P_3 and P_4 (see Fig. 3a). The resonance corresponding to P_3 (dotted line) red-shifts as R_{bead} increases. This is in agreement with the expected red-shift of the LSP resonance of the triangles as their size (or equivalently R_{bead}) increases.[29] On the other hand, the invariance of 2θ ensures a practically unchanged spectral position of the absorption peak corresponding to P_4 (dashed-dotted line), although R_{bead} and 2d (see Fig. 1b) vary over a large range. As expected from previous studies,[30] the focusing of the electromagnetic energy at the end of tapered tips is sensitive only to the tip opening angle. The spectral position of this absorption peak determines the upper cut-off of the absorption band and as seen in Fig. 2b can be greatly increased by decreasing the tip angle, 2θ.

In order to assess the performance of our concept in absorbing the solar spectrum, we calculate the total absorption as

$$A_{tot} = \frac{\int_{350\,nm}^{1000\,nm} A(\lambda)I(\lambda)\mathrm{d}\lambda}{\int_{350\,nm}^{1000\,nm} I(\lambda)\mathrm{d}\lambda}$$

where $A(\lambda)$ and $I(\lambda)$ are the absorption of the structure and the solar irradiance for the standard AM1.5 (air mass) spectrum, respectively. In calculating the above absorption we consider the spectral range of 350–1000 nm, within which we performed measurements and simulations. The discarded part contains around 25% of the total solar energy. The contour plot in Fig. 3c shows the simulated total absorption as a function of thickness of the SiO_2 layer, h_{SiO_2}, and the size of the beads used for NSL, R_{bead}. In these simulations we used a constant value for $\Delta R/R_{bead}$ (= 0.0133, corresponding to $\Delta R = 2$ nm at $R_{bead} = 150$ nm), to ensure a constant angle at the tips of the triangles,

2θ. Based on the above-mentioned studies, this assumption ensures almost the same upper cut-off wavelength of the absorption band for all the cases. The optimal geometry with $R_{bead} = 200$ nm and $h_{SiO_2} = 45$ nm leads to a total absorption of 84%. As explained before (see Fig. 2b), smaller values for ΔR can lead to substantially broader absorption spectra and therefore increase the total absorption. Furthermore, Fig. 3c shows that the total absorption around the optimum is quite insensitive to h_{SiO_2} and R_{bead}, making the performance of such a device highly tolerant to fabrication imperfections.

Conclusions

In conclusion, exploiting a combination of different plasmonic absorption phenomena in an array of tapered triangles integrated in an MIM configuration, we introduced a novel ultra-broadband plasmonic absorber with average absorption 88% within the spectral range of 380–980 nm. In addition, this absorber is insensitive to both light polarization and angle of incidence. While aspects of light absorption by arrays of tapered triangles have been studied before, our results contain significant novelty based on exploiting simultaneously four distinct absorption phenomena (each of different nature) two of which are accessible only through the MIM configuration. By suitably selecting a host of geometrical dimensions, we managed to harvest the collective benefit of these absorption events and pieced together a continuous absorption band. Our simulations show that one could go even beyond these high values, in terms of broadness and total absorption, by fine-tuning the geometrical parameters, specifically the tip regions of the tapered triangles in the pattern. Importantly, in contrast to previous successful designs, the fabrication of our concept is based on NSL which is a low-cost and easily accessible method.[21,23] Although monocrystallinity is not a stringent requirement in our design, achieving large defect-free crystals with NSL remains a challenge. This bottleneck has been addressed in recent studies[31,32] and significant improvements are foreseen. To this end, and based on the nano-scale thickness (260 nm) of our design, we envision the up-scaling of the absorber on flexible substrates even in a roll-to-roll manner. Being ultra-thin, the absorber can efficiently and rapidly elevate the temperature within a nano-scale layer, which can be exploited in various applications such as micro-fluidics,[33] solar thermoelectrics[4,9,34] and high temperature chemical reactions.[35] In addition, efficiently absorbing the extremely broad solar light and concentrating it at the very end of the tips renders the present concept an interesting candidate for enhancing solar-based photochemistry and improving the efficiency of solid-state devices.[5–8]

References

1 H. A. Atwater and A. Polman, *Nat. Mater.*, 2010, **9**, 205–213.
2 J. V. van de Groep, P. Spinelli and A. Polman, *Nano Lett.*, 2012, **12**, 3138–3144.
3 C. H. Wu, B. Neuner, J. John, A. Milder, B. Zollars, S. Savoy and G. Shvets, *J. Opt.*, 2012, **14**, 024005.

4 Y. J. Xiong, R. Long, D. Liu, X. L. Zhong, C. M. Wang, Z. Y. Li and Y. Xie, *Nanoscale*, 2012, **4**, 4416–4420.

5 S. C. Warren and E. Thimsen, *Energy Environ. Sci.*, 2012, **5**, 5133–5146.

6 S. Linic, P. Christopher and D. B. Ingram, *Nat. Mater.*, 2011, **10**, 911–921.

7 F. M. Wang and N. A. Melosh, *Nano Lett.*, 2011, **11**, 5426–5430.

8 M. W. Knight, H. Sobhani, P. Nordlander and N. J. Halas, *Science*, 2011, **332**, 702–704.

9 D. Kraemer, B. Poudel, H. P. Feng, J. C. Caylor, B. Yu, X. Yan, Y. Ma, X. W. Wang, D. Z. Wang, A. Muto, K. McEnaney, M. Chiesa, Z. F. Ren and G. Chen, *Nat. Mater.*, 2011, **10**, 532–538.

10 A. Moreau, C. Ciraci, J. J. Mock, R. T. Hill, Q. Wang, B. J. Wiley, A. Chilkoti and D. R. Smith, *Nature*, 2012, **492**, 86–89.

11 M. K. Hedayati, M. Javaherirahim, B. Mozooni, R. Abdelaziz, A. Tavassolizadeh, V. S. K. Chakravadhanula, V. Zaporojtchenko, T. Strunkus, F. Faupel and M. Elbahri, *Adv. Mater.*, 2011, **23**, 5410–5414.

12 M. Elbahri, S. Homaeigohar, R. Abdelaziz, T. Dai, R. Khalil and A. U. Zillohu, *Adv. Funct. Mater.*, 2012, **22**, 4771–4777.

13 A. De Luca, N. Depalo, E. Fanizza, M. Striccoli, M. L. Curri, M. Infusino, A. R. Rashed, M. La Deda and G. Strangi, *Nanoscale*, 2013, **5**, 6097–6105.

14 K. Aydin, V. E. Ferry, R. M. Briggs and H. A. Atwater, *Nat. Commun.*, 2011, **2**, 517.

15 M. G. Nielsen, A. Pors, O. Albrektsen and S. I. Bozhevolnyi, *Opt. Express*, 2012, **20**, 13311–13319.

16 A. Aubry, D. Y. Lei, A. I. Fernandez-Dominguez, Y. Sonnefraud, S. A. Maier and J. B. Pendry, *Nano Lett.*, 2010, **10**, 2574–2579.

17 J. B. Pendry, A. Aubry, D. R. Smith and S. A. Maier, *Science*, 2012, **337**, 549–552.

18 E. E. Narimanov and A. V. Kildishev, *Appl. Phys. Lett.*, 2009, **95**, 041106.

19 T. Sondergaard, S. M. Novikov, T. Holmgaard, R. L. Eriksen, J. Beermann, Z. H. Han, K. Pedersen and S. I. Bozhevolnyi, *Nat. Commun.*, 2012, **3**, 969.

20 T. Sondergaard and S. I. Bozhevolnyi, *New J. Phys.*, 2013, **15**, 013034.

21 J. C. Hulteen and R. P. Vanduyne, *J. Vac. Sci. Technol., A*, 1995, **13**, 1553–1558.

22 B. J. Y. Tan, C. H. Sow, T. S. Koh, K. C. Chin, A. T. S. Wee and C. K. Ong, *J. Phys. Chem. B*, 2005, **109**, 11100–11109.

23 X. Y. Zhang, A. V. Whitney, J. Zhao, E. M. Hicks and R. P. Van Duyne, *J. Nanosci. Nanotechnol.*, 2006, **6**, 1920–1934.

24 S. R. Ye, A. L. Routzahn and R. L. Carroll, *Langmuir*, 2011, **27**, 13806–13812.

25 E. D. Palik and G. Ghosh, *Handbook of optical constants of solids*, Academic Press, San Diego, 1998.

26 N. Liu, M. Mesch, T. Weiss, M. Hentschel and H. Giessen, *Nano Lett.*, 2010, **10**, 2342–2348.

27 Y. Z. Chu and K. B. Crozier, *Opt. Lett.*, 2009, **34**, 244–246.

28 W. Rechberger, A. Hohenau, A. Leitner, J. R. Krenn, B. Lamprecht and F. R. Aussenegg, *Opt. Commun.*, 2003, **220**, 137–141.

29 K. L. Kelly, E. Coronado, L. L. Zhao and G. C. Schatz, *J. Phys. Chem. B*, 2003, **107**, 668–677.

30 Y. Luo, J. B. Pendry and A. Aubry, *Nano Lett.*, 2010, **10**, 4186–4191.

31 G. D. Moon, T. I. Lee, B. Kim, G. Chae, J. Kim, S. Kim, J. M. Myoung and U. Jeong, *ACS Nano*, 2011, **5**, 8600–8612.

32 C. C. Ho, P. Y. Chen, K. H. Lin, W. T. Juan and W. L. Lee, *ACS Appl. Mater. Interfaces*, 2011, **3**, 204–208.

33 J. S. Donner, G. Baffou, D. McCloskey and R. Quidant, *ACS Nano*, 2011, **5**, 5457–5462.

34 K. Moth-Poulsen, D. Coso, K. Borjesson, N. Vinokurov, S. K. Meier, A. Majumdar, K. P. C. Vollhardt and R. A. Segalman, *Energy Environ. Sci.*, 2012, **5**, 8534–8537.

35 C. Fasciani, C. J. B. Alejo, M. Grenier, J. C. Netto-Ferreira and J. C. Scaiano, *Org. Lett.*, 2011, **13**, 204–207.